Recording the angular dispersion of a terahertz beam into its frequency spectrum for fast measurements

YONGPENG HAN,[1] JIAYU ZHAO,[1,*] QINING WANG,[1] JIAAO YAN,[1] YAO YAO,[1] JIAHAO XIAO,[1] CHANG LIU,[2] FEIFAN ZHU,[1] LI LAO,[3] AND YAN PENG[1,4] (iD)

[1]*Terahertz Technology Innovation Research Institute, Terahertz Spectrum and Imaging Technology Cooperative Innovation Center, Shanghai Key Lab of Modern Optical System, University of Shanghai for Science and Technology, Shanghai 200093, China*
[2]*Shanghai Institute of Optics and Fine Mechanics, Chinese Academy of Sciences, Shanghai 201800, China*
[3]*Tera Aurora Electro-Optics Technology Co., Ltd, Shanghai 200093, China*
[4]*Shanghai Institute of Intelligent Science and Technology, Tongji University, Shanghai 200092, China*
[*]*zhaojiayu@usst.edu.cn*

Abstract: The frequency-dependent divergence angle of terahertz (THz) beams is a crucial aspect in understanding the generation and transmission of broadband THz waves. However, traditional beam profiling methods, such as 1D or 2D translation/rotation scanning detection, are time-consuming and wasteful of THz energy, making them unsuitable for fast measurement applications, such as single-shot THz generation and detection. Here, we proposed a simple solution that involves passing the THz beam through a core-anti-resonant reflective (CARR) cavity (e.g., a paper tube). The spatial information of the beam is then recorded into its frequency spectrum, which can be easily detected by a following traditional THz time-domain spectroscopy (TDS) system or a single-shot sampling setup. Our method enables the acquisition of the angular dispersion without repetitive measurements, and represents a significant step forward in fast and efficient achievement of spatial properties of broadband THz beams.

1. Introduction

The frequency-resolved angular distribution of terahertz (THz) beams is an essential element towards understanding the generation mechanism of broadband THz waves from sources like single- [1–7] or two-color femtosecond laser filaments [8–13], as well as managing the THz diffraction propagation in free space [14–17], etc. Generally, the THz angular dispersion pattern can be achieved by beam profiling methods, including the knife-edge (KE) technique along the radial direction of the beam [13,18,19], the rotated sampling around the beam axis [1–6,20], and the scanning imaging of the beam's cross section [21,22]. In addition, narrowband THz filters were frequently positioned before THz detectors (e.g., cameras [8,23] or bolometers [1,3,4]) in order to resolve different frequency components.

However, the aforementioned approaches suffered from repetitive experimental operations, such as 1D or 2D translation/rotation scanning detection or optical devices switchover, which were quite time consuming and THz energy wasting. This issue becomes even more unacceptable under conditions that require fast measurements. For example, in the single-shot scheme [24–26], a single THz pulse is emitted during a transient process and must be captured in a single measurement, as opposed to using multiple pulses and measurements to buildup an image or spectrum. In this case, the angular dispersion of the THz radiation can hardly be figured out.

In this work, we proposed a straightforward solution to this problem by transmitting the studied THz beam (in band of 0.1-1.2 THz) through a core-anti-resonant reflective (CARR)

cavity [27,28] such as a paper tube, inside which the beam's angular information was recorded into its frequency spectrum. Next, the output THz pulse was detected by a conventional THz time-domain spectroscopy (TDS) system, and the modulated spectrum was retrieved by Fourier transformations (FT) on the temporal signal. By this means, the frequency-resolved angular distribution was easily obtained with a single THz pulse avoiding repetitive measurements. Hence, our method is promising to pave the way towards fast acquisition of the spatial property of broadband THz beams.

2. Conventional methods for detecting the angular dispersion (θ-f) of a THz beam

For a typical Gaussian beam emitted from a THz transmitter module combined by a photoconductive antenna (PCA) and two TPX lenses, the divergence angle (φ) can be defined as the included angle between one cone-beam ray and the axis z as shown in Fig. 1(a). And the φ value can be estimated by conventional methods like the knife-edge (KE) measurement or 2D scanning imaging at different longitudinal locations. For the former, please see Section 6. For the latter, we traced the cross-sectional spots of the beam. Figure 1(b) displayed five examples of transverse THz images at $z = -5$, 0, 5, 10 and 15 mm, respectively, and the smallest spot size
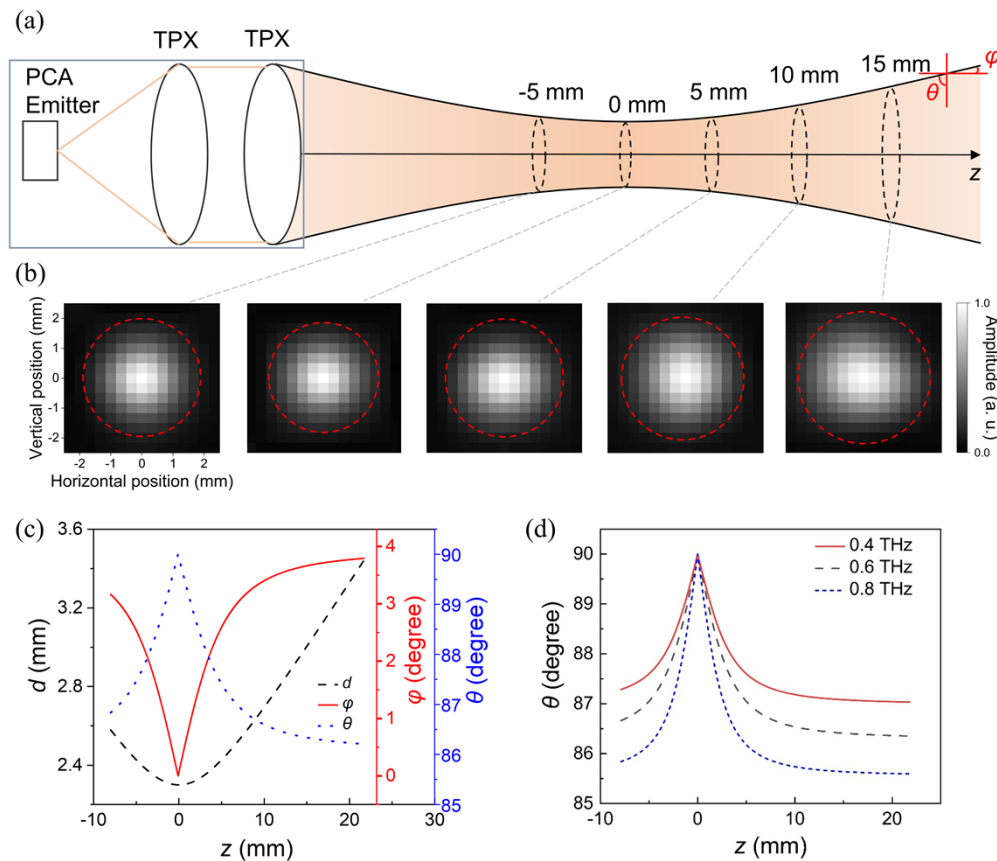

Fig. 1. (a) Schematic of a THz beam emitted from a THz transmitter module. (b) Five cross-sectional amplitude distributions of the THz beam via scanning imaging. (c) Evolutions of the beam diameter d, the divergence angle φ and the complementary angle θ along the axis z. (d) θ at three THz frequencies.

was located at $z = 0$ mm as the beam waist. The scanning THz imaging was performed by a self-built micro-probe-based THz imaging system [29], which enables the scanning imaging of THz distributions within different longitudinal cross-sections of the THz beam, and at each pixel, a time-domain THz waveform was recorded. In Fig. 1(b), the value of each pixel was determined by the peak-to-peak amplitude of the temporal THz waveform. Although the probe resolution of this system is as high as 50 μm, the scanning step size used in our study was relatively large (15×15 pixels in 5×5 mm), because our THz beam spot was simply in a Gaussian shape without micro-structures. On the other hand, it was for saving time.

The spot diameter d (at $1/e$) along z has been quantified as the black dashed line in Fig. 1(c), and φ was calculated by $\varphi = \arctan(\Delta d/2\Delta z)$ as shown as the red solid line in the same figure. It can be seen that this THz beam had a loose divergence with the maximum φ of about 4 degree. This beam configuration was set for simulating the THz emission from optical filaments which is normally in a cone angle of several degrees [8,10,11]. By now, the THz beam has been profiled in a traditional way, and related parameters were also used for establishing the THz source during our simulations with the software Rsoft (Section 4).

On the other hand, the proposed CARR method is sensitive to θ ($= 90\text{-}\varphi$) as shown in Fig. 1(a) and 2. Therefore, for the sake of convenience for analyses, we added a θ line ($\theta = 90\text{-}\varphi$) in Fig. 1(c) as the blue dotted line. In this way, one can see that this θ distribution is actually achieved from Fig. 1(b), i.e., from the THz peak-to-peak amplitude image. Furthermore, if we abstract the spectral amplitude of the THz signal at a certain frequency rather than the time-domain peak-to-peak amplitude for each pixel value of THz images, we would get an evolution of THz images at this frequency along the z axis. Then, we could calculate the frequency-resolved θ line as we did in Fig. 1(c). Three examples at 0.4, 0.6 and 0.8 THz were plotted in Fig. 1(d). Two conclusions can be drawn in view of this figure: (I) About the angular dispersion (θ-f), θ is smaller at a higher frequency at a fixed z, which is the central concern of our simulations and experiments carried out by the CARR method in Section 4. (II) For a specific frequency, θ gradually decreased along z, which has also been studied in Section 5.
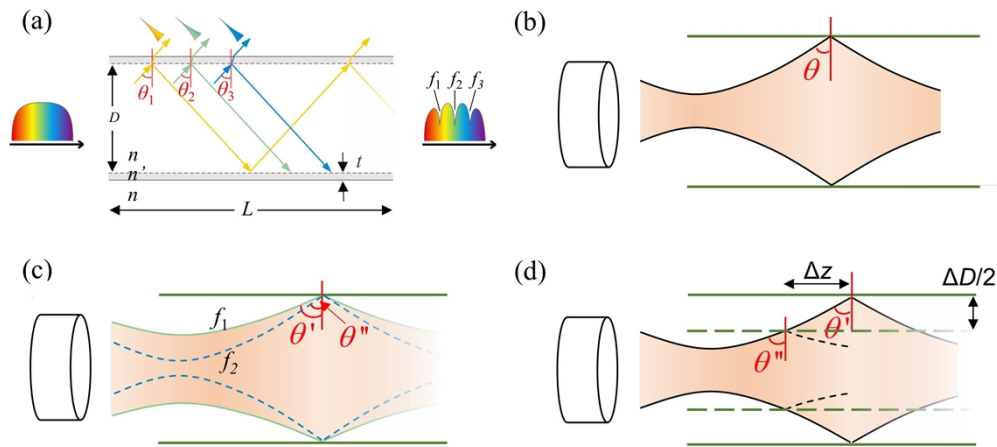

Fig. 2. (a) The CARR principle. (b-d) A Gaussian beam was transmitted along the CARR cavity for measuring θ of different frequencies along the propagation direction z.

3. Principle of the CARR technique

The geometrical optical mechanism of CARR can be understood in Fig. 2(a): optical rays in a broad THz band oscillate inside a thin-wall cavity (e.g., a paper tube), and the output THz

spectrum has quasi-periodic dips as resonant frequencies f_m [27,28] given by

$$f_m = \frac{mc}{2nD \cos \theta_m} \qquad (1)$$

where $m = 1, 2, 3\ldots$ is the resonance order, c is the speed of light in vacuum, n (= 1 for air) is the refractive index inside the cavity, D is the inner diameter of the tube, and θ_m is the incidence angle of light on the inner surface of the cavity. Based on Eq. (1), θ_m can be easily computed by

$$\theta_m = \arccos \left(\frac{c}{2D} \left/ \frac{f_m}{m} \right. \right) \qquad (2)$$

Therefore, the spatially angular dispersion, i.e., θ-f, can be obtained by merely detecting the transmitted THz-CARR spectrum.

Figure 2(b) indicates the actual scenario of a Gaussian beam incidence into the CARR cavity from a THz source and the corresponding θ to be considered. By utilizing this pattern, we can verify both conclusions (I) and (II) presented in Section 2, as demonstrated in Fig. 2(c) and (d), respectively. Briefly, in Fig. 2(c), the varied θ at different frequencies can be determined. And in Fig. 2(d), the varied θ along z at one certain frequency can be confirmed by changing the inner diameter D of the CARR tube.

4. Simulated and experimental results of the THz angular dispersion (θ-f)

To begin with, simulations have been performed with a numerical model established by the commercial software Rsoft [27,28]. The paper tube model and the modal cross section built in Rsoft are displayed in Fig. 3(a) and (b), respectively, with $n = 1$ (air), $n' = 1.6$ (paper, close to that in Ref. [30]), $t = 80\,\mu$m (paper wall thickness), $L = 15$ cm (tube length) and $D = 10.5$ mm (inner diameter), which is the mean value of the used tubes in following experiments (Fig. 4,5). Also in the software, the input light source was set in Gaussian mode with width of 2.5 mm and θ around 85 degree.

The simulated THz transmission spectrum is shown in Fig. 3(c), and clear CARR phenomena, i.e., resonant frequencies f_m dips ($m = 1, 2, 3, 4$ and 5, highlighted by red dashed lines) can be observed as expected in Fig. 2(a). Subsequently, the five f_m are extracted and shown in Fig. 3(d) as symbols. The connecting line of each symbol with the coordinate (0, 0) has a slope of f_m/m. According to Eq. (2), θ_m (at f_m) is positively correlated with f_m/m, thus, determined by the varied line slopes in Fig. 3(d). Theoretically in this way, the angular dispersion θ_m-f_m can be resolved. To verify this point, experiments were performed as follows.

The THz beam to be measured was shown in Fig. 1(a), which was emitted from a THz transmitter module as a group of a photoconductive antenna emitter (PCA, from MenloSystems) and two THz converging lenses (TPX). The employed cage module was able to maintain the alignment of these three optical devices. So did the detection module. Between the two modules, a rail and linkage system was also adopted to ensure collimation. The THz focus was fixed at $z = 0$ mm, and the CARR cavity was placed with the tube entrance coinciding with the waist position of the THz beam for detecting its angular divergence as shown in Fig. 4(a). The other parts in Fig. 4(a) demonstrate our all-fiber THz time-domain spectroscopy system (TDS). That is, a fiber laser device (LangYanTech) delivered laser pulses with central wavelength of 1550 nm, duration of 100 fs, average power of 60 mW and repetition frequency of 100 MHz in two paths as pump and probe, respectively. The pump/probe laser pulses passed through polarization-maintaining fibers (PMF) and excited the THz transmitter/detection module. Besides, an optical delay line (General Photonics) was mounted in the probe path.

The used CARR cavities (Fig. 4(b)) included a single-layer paper tube (used in this section) with parameters similar with the above simulation, and a pair of half tubes (used in the next section) made by 3D printing with $n' = 1.64$ (resin) and $t = 3$ mm. These two kinds of tubes
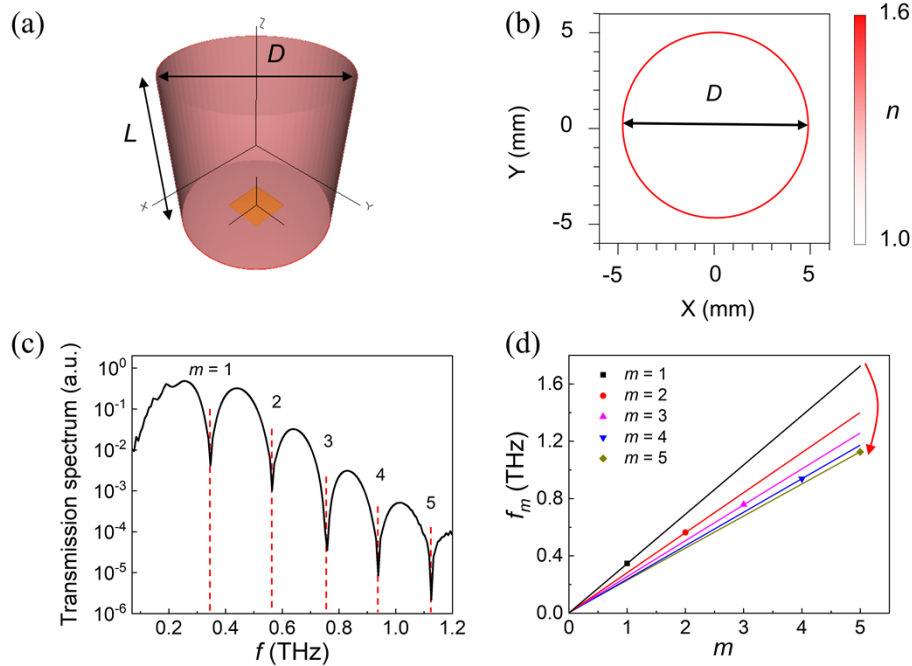
Fig. 3. Simulations of the CARR mechanism: (a) the paper tube model, (b) the modal cross section, (c) the transmission spectrum and (d) its five resonant frequencies.

were used in two separate experiments, and the advantage of the resin tube is the adjustable *D* by independent translation of each half tube as displayed in the bottom right corner of Fig. 4(b). It is worth noting that, the cylindrical paper-tube cavities in our experiments were manufactured by using standard molds [27], and their repositioning accuracy was also taken into consideration in our setup. There are front and rear adjustable apertures and holders, enabling the tube to be repositioned as needed, as did in Ref. [31].

Moreover, the top left corner of Fig. 4(b) presents the incident time-domain THz pulse into the paper cavity. Compared with standard waveforms in the THz-TDS spectrometer [32], ours had a slight distortion due to the dispersion of pumping laser pulses in our all-fiber THz-TDS system. The output THz pulse is shown in Fig. 4(c) together with the FT spectrum. It can be seen that there are five resonant frequencies, and the corresponding f_m/m decreased as shown as the line slopes in Fig. 4(d), similar with the simulation outcomes in Fig. 3. While it is worth mentioning that, small discrepancies between the experimental and simulated f_m can be attributed to the fabrication errors of the paper tube diameter, which was about 10.7 mm. Besides, there still existed a gap between the numerically constructed Gaussian beam and the experimental one. This might also contribute to the discrepancy. Note that, the tube wall thickness *t* will not directly affect the observed f_m locations [27] according to Eq. (1) where *t* is not involved.

Based on Fig. 4(d) and Eq. (2), the calculated *θ-f* are shown in Fig. 4(e), which decreased from 87.5 to 86.7 degree with the increasing THz frequency (below 1.2 THz). This achievement is basically consistent with the point (I) of Fig. 1(d) in Section 2, whose *θ* value decreased around 87 degree in the THz range from 0.4 to 0.8 THz. Through multiple measurements, we have also added error bars to the experimental f_m data (Fig. 4(d)). Specifically, the first two points (*m* = 1, 2) remain nearly unchanged, while the last three points (*m* = 3, 4, 5) exhibit slight fluctuations (±0.008 THz). This means the f_m value had a maximum change around a spectral resolution, which is approximately 0.016 THz given by the total temporal width (64 ps) of the detected THz
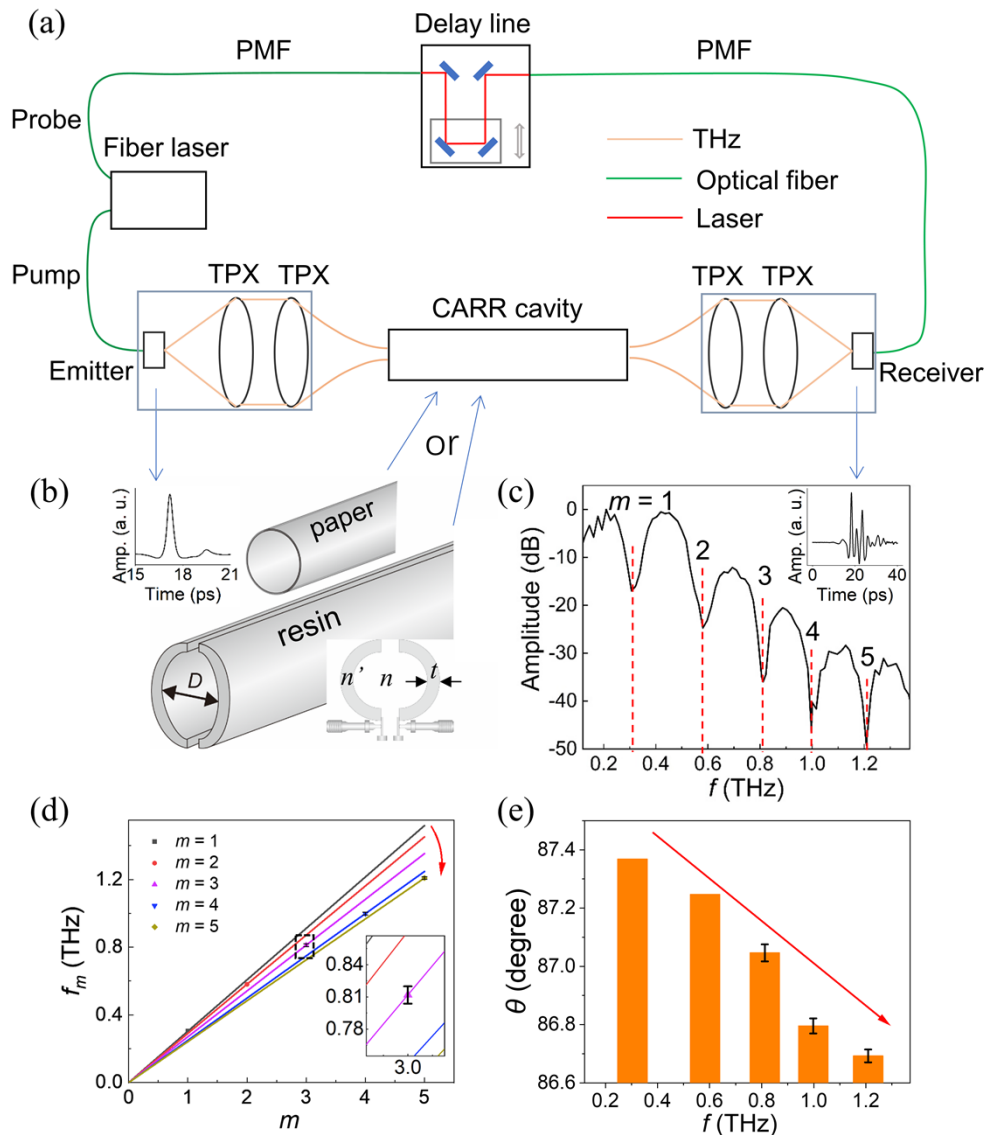
Fig. 4. (a) The experimental setup for measuring the frequency-resolved angular distribution of the THz beam by the CARR method. (b) The used CARR cavities made of paper or resin, respectively. Insets: the input THz pulse and the transverse image of the resin cavity. (c) The transmission THz spectrum of the paper cavity. Inset: the output THz pulse. (d) Resonant frequencies of the CARR phenomena. (e) The calculated θ-f by data in (d) and Eq. (2).

waveform. The impact of this f_m error on the θ angle error is depicted in Fig. 4(e), showing no alteration to the overall trend. So far, both simulations and experiments have proved the validity of the CARR cavity on angular dispersion recording on the THz spectrum. All the signal that needs to be detected is a single THz pulse (Fig. 4(c)), which has significantly sped up the measurement process. In similar ways, two additional experiments have been carried out in Section 7 and 8, further making the proposed CARR method convincing.
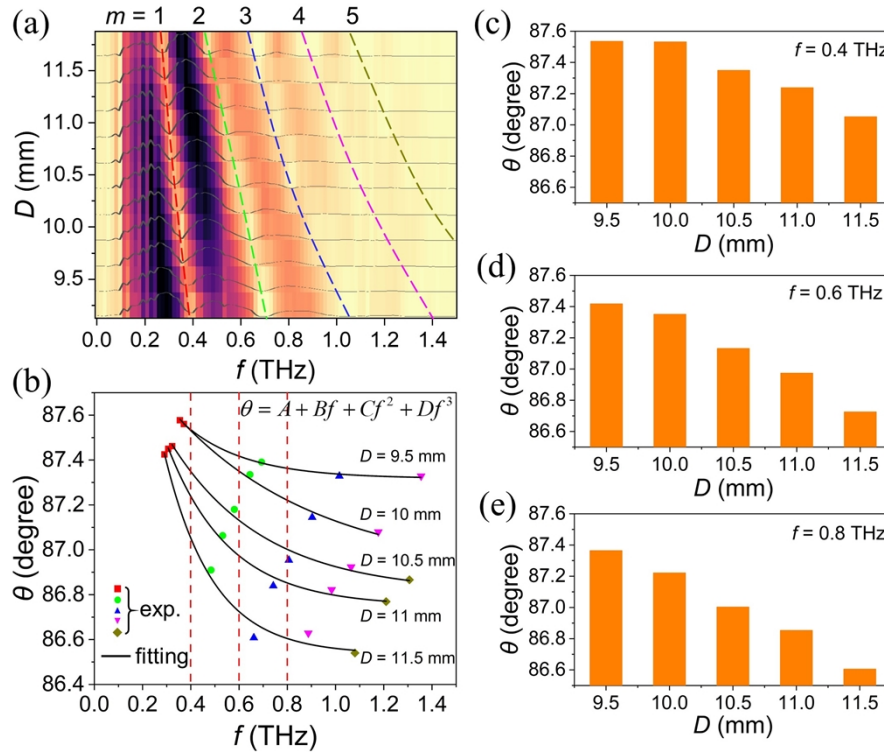
Fig. 5. (a) The CARR spectra with varied cavity diameters. (b) The calculated θ-f by data in (a) and Eq. (2). (c-e) The extracted θ-D relations from (b) at 0.4, 0.6 and 0.8 THz.

5. Additional measurements of the θ-z relationship

In order to verify the conclusion (II) of θ-z in Fig. 1(d), we measured the transmitted THz spectra with the 3D printing cavity by varying its D from 9 to 12 mm. Note that, $\Delta D = 1$ mm resulted into $\Delta z \sim 10$ mm for $\theta = 87$ degree as shown in Fig. 2(d). The spectral results are shown in Fig. 5(a), inside which the trajectories of f_m were highlighted by dashed curves at different m. Performing similar calculations like that from Fig. 4(c) to (e), we obtained θ-f values from Fig. 5(a) and presented parts of the results in Fig. 5(b) as symbols with D ranging from 9.5 to 11.5 mm in step length of 0.5 mm. Note that, symbols in the same shape and color corresponded to the same resonance order m (dashed line) in Fig. 5(a).

In Fig. 5(b), it can be clearly seen that θ decreased with the increasing f at a certain D, like that in Fig. 4(e), and this trend has been further polynomially fitted by black lines ($\theta = A + Bf + Cf^2 + Df^3$). Next, on these fitting curves, we extracted the θ values along three vertical dashed lines (at 0.4, 0.6, 0.8 THz) and plotted the data in Fig. 5(c-e), respectively, illuminating the decline of overall θ bars towards higher frequencies. Furthermore, under each frequency, θ gradually decreased with the growth of D (i.e., the increasing z, as shown in Fig. 2(d)), which agrees with the point (II) of Fig. 1(d) in Section 2.

6. Comparison experiment of KE measurements

In the above works, the THz beam has been profiled by two methods. One is the conventional 2D scanning imaging as shown in Fig. 1(b-d). And the other one is the proposed CARR technique. All the comparisons were performed between these two methods' results, proving

the CARR's accuracy and efficiency on divergence angle detection. Here, we also carried out another comparative experiment using the traditional knife-edge (KE) method.

This time, a thin aluminous (Al) sheet was 1-D scanned across the THz beam spot at $z = 0$ and 10 mm, respectively. The experimental results and corresponding error function fittings are respectively shown in Fig. 6(a) and (c), inside which one can see the decreasing THz amplitude (within 0.1-1 THz) as a function of the displacement distance of the Al sheet. Figure 6(b) and (d) are enlarged details around the displacement distance of 0 mm in Fig. 6(a) and (c). To quantificationally analyze the fitting effect of the error function, the root mean squared error as $\mathrm{RMSE}(x_i, X_i) = \sqrt{\frac{1}{n} \sum_{i=1}^{n} (x_i - X_i)^2}$ was used to estimate the matching between experimental and
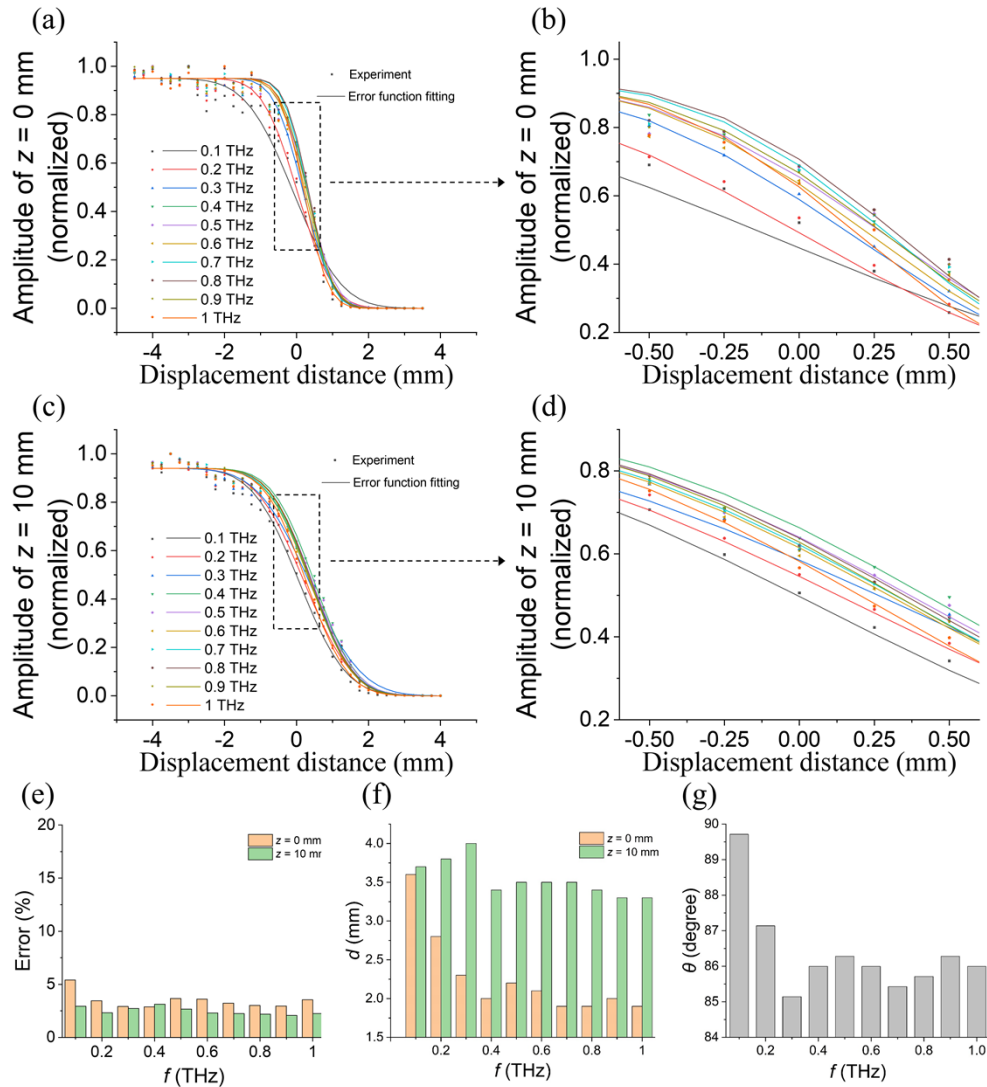

Fig. 6. Normalized frequency-divided THz amplitude measured by the KE method and fittings within 0.1-1 THz at (a-b) $z = 0$ mm and (c-d) $z = 10$ mm, respectively. (e) Errors of the fittings in (a) and (c) at different frequencies. (f) The THz spot diameters at $z = 0$ mm and $z = 10$ mm measured by the KE method, and (g) the calculated θ at each THz frequency.

fitted data. Here, n is the number of samples for each frequency, and x_i is each sample value of experiment, and X_i is that of fitting. Figure 6(e) displays the calculated fitting error values, most of which can be observed below 5%. In Fig. 6(e), it is also noticed that the overall errors at $z = 0$ mm are slightly larger than those at $z = 10$ mm. This is because of the more oscillations in the knife-edge curves at $z = 0$ mm (Fig. 6(a)). And these unwanted oscillations might arise due to the diffraction effect. Since at the THz beam focus (with a smaller THz spot size), the diffraction effect during knife-edge measurements was also stronger.

Subsequently, the THz spot diameters at each frequency were extracted and shown in Fig. 6(f), where the spot sizes at $z = 10$ mm were larger than those at $z = 0$ mm as expected. The corresponding θ value can be calculated by $\theta = 90 \text{-} \varphi = 90 \text{-arctan}(\Delta d / 2 \Delta z)$, where $\theta + \varphi = 90$ is shown in Fig. 1(a), Δd is the difference between THz spot diameters at $z = 10$ and 0 mm, and $\Delta z = 10$ mm. Finally, the θ results are shown in Fig. 6(g). It can be seen that θ is around 86 degree, in agreement with the CARR's data (Fig. 4). However, the frequency dependence of θ is not well observed with this KE measurement. In a word, for obtaining the frequency-dependent divergence angle of THz beams, traditional approaches such as the imaging method (Fig. 1) and the KE skill (Fig. 6) require 1D or 2D transverse scanning at multiple longitudinal positions z, which are time consuming, THz energy wasting, and applicable to limited situations. By contrast, our CARR method is much more efficient.

7. Supplementary experiments of the CARR method on a larger angular distribution of the THz beam

We introduced an extra TPX lens to enhance the THz beam focusing (Fig. 7(a)), thereby increasing the divergence angle to about 2 degrees, which can also be resolved by our CARR method as shown in Fig. 7(b-d).
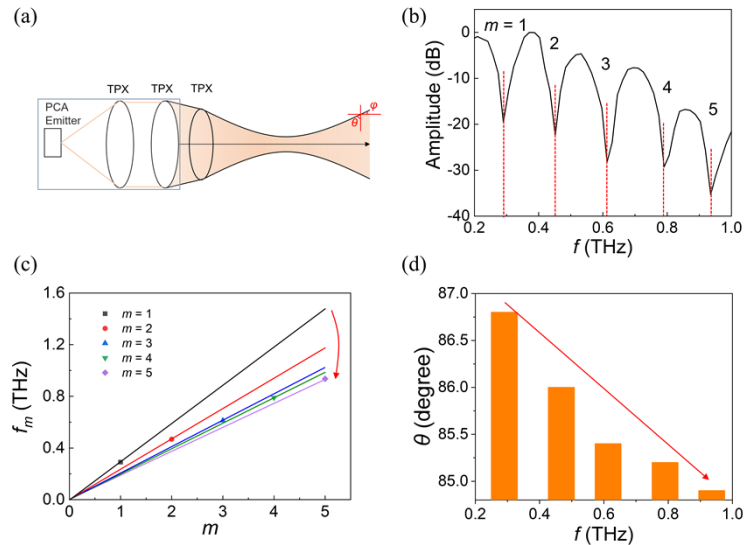

Fig. 7. An additional TPX lens was introduced to enhance the divergence angle to about 2 degrees, detected by our CARR method.

8. Supplementary experiments of the CARR method on a laser-plasma-filament based THz source

We also conducted experiments on another widely used THz source, namely femtosecond laser filamentation. Briefly, a repetition rate of 1 kHz, central wavelength of 800 nm and duration of 100 fs Ti: sapphire laser pulse with energy of 1 mJ/pulse was focused by a lens with focal length of 30 cm. After the lens, a 0.1-mm-thick Type-I β-barium borate (BBO) crystal for frequency doubling was inserted into the pump path. The air was ionized at the laser focus and a 7-mm-length plasma filament was generated. Subsequently, the THz wave emitted from the filament was detected by our CARR method. The central axis of the paper tube had coincided with the optical axis, and the midpoint of the filament was located at the entrance of the tube. The experimental results revealed an increasing trend of the detected θ angle with respect to the frequency (Fig. 8), which differs from the PCA experiments but aligns with the conclusions in field of THz radiation induced by laser filamentation given by the well-known off-axis phase matching [8]. Thus, our CARR approach is deemed feasible.
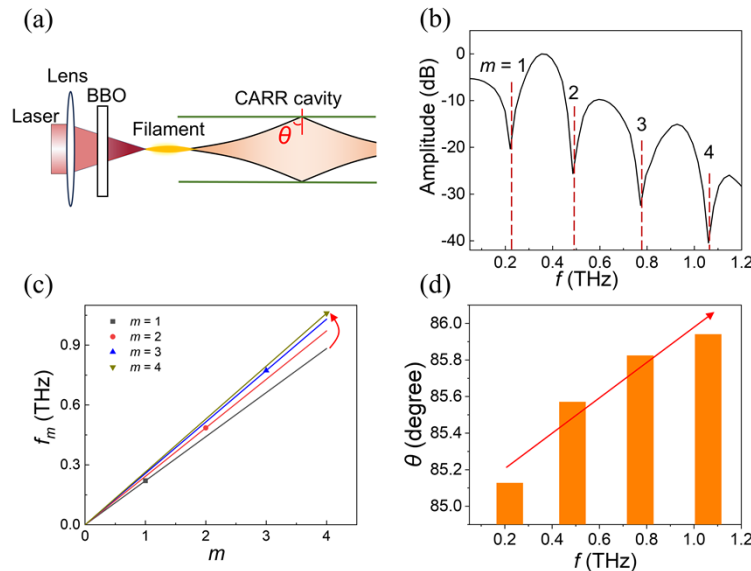

Fig. 8. THz radiation from a laser plasma filament detected by our CARR method.

9. Discussion

It should be noticed that while the CARR method has successfully replicated the beam profile features marked as (I) and (II), the detected θ values using CARR were not exactly the same as those shown in Fig. 1(d). Specifically, for 0.8 THz in Fig. 5(e), θ ranged from 87.4 to 86.6 degree, whereas Fig. 1(d) showed a minimum θ value of approximately 85.5 degrees. One possible reason for this quantitative discrepancy could be due to the diffraction experienced by the THz wave during oscillated propagation inside the cavity, as a result of its large wavelength (sub-mm). Consequently, the THz beam cannot be totally considered as ideal optical rays (Fig. 2(a)), which makes Eq. (1,2) less precise in this situation. Moreover, for a Gaussian spot, the divergence angle is a fuzzy parameter depending on the diameter definition. Thus, the results might be more accurate if the THz radiation has a conical shape with an off-axis maximum, also known as a donut mode.

On the other hand, the presented CARR phenomena in this work (i.e., periodic dips in the spectrum) has similarities with the typical ARROW theory [33,34], or the multi-mode interference inside a hollow-core waveguide [35,36]. However, the possibility of these two effects can be ruled out for our phenomenon. For the former, please see our previous work [27], which indicates the connections between the F-P concept, our CARR and also the ARROW mechanisms. For the latter, as put in Ref. [35,36], the used tube walls were opaque for optical waves (or THz waves), which were blocked from transmitting through the cladding. For example, in the former work, a metallic tube wall was employed for the multimode interference of THz waves within the tube core.

Following this clue, assuming that previously multimode interferences occurred inside our paper tubes, then there would still be spectral dips output if we change the paper material into metal. However, as can be seen in top of Fig. 4(b) of our work [27], the spectral dip phenomenon was not observed with a metallic tube. We also carried out Rsoft simulations on a Ag-wall tube, which did not work either (Fig. 9). Whereas under the same simulation conditions, a paper tube exhibits dips in the spectrum (Fig. 3(c)). So did a meshy metallic tube or a PVC plastic tube in our experiments [27]. This is because both the transparency and reflection of THz waves by the tube cladding are necessary for the CARR theory. In other words, for our cases, the interference outside the tube wall is more crucial than inside the tube core, which is clearly resulted from the leaky F-P effect as the origin of our CARR theory. Therefore, the multi-mode interference effect cannot play a dominate role in this work.
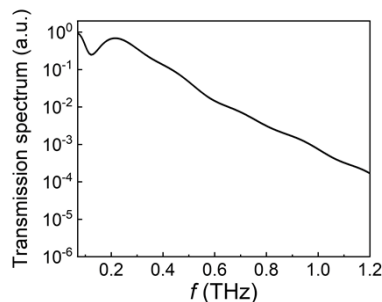

Fig. 9. Rsoft simulations of a metallic (Ag) tube for THz transmission based on the CARR theory. All simulated conditions were the same for this figure and Fig. 3(c) except for the cladding materials.

10.   Conclusion

In summary, this work has proposed a simple method for recording the angular dispersion information of a THz beam into its frequency spectrum by using a CARR cavity. The output THz transient has a pulse duration of approximately 20 ps (inset of Fig. 4(c)) and can be captured by either a common THz-TDS or a single-shot THz detection setup coupled with the CARR cavity. From the FT spectrum of the THz pulse, the beam divergence angle at the resonant frequencies can be easily calculated, thus enabling fast determination of the angular dispersion trend. The development of this CARR technology has the potential to advance the field of real-time THz beam profiling with high temporal resolution, and facilitate the progress of THz generation and propagation [37–39].

Disclosures. The authors declare no conflicts of interest.

Data availability. Data underlying the results presented in this paper are not publicly available at this time but may be obtained from the authors upon reasonable request.

References

1. G. E. Rizaev, L. V. Seleznev, D. V. Mokrousova, D. V. Pushkarev, and A. A. Ionin, "Terahertz emission pattern from a single-color filament plasma," Opt. Lett. **47**(22), 5917 (2022).
2. A. V. Koribut, G. E. Rizaev, D. V. Mokrousova, S. A. Savinov, A. A. Reutov, Y. A. Mityagin, L. V. Seleznev, and A. A Ionin, "Similarity of angular distribution for THz radiation emitted by laser filament plasma channels of different lengths," Opt. Lett. **45**(14), 4009 (2020).
3. I. A. Nikolaeva, D. E. Shipilo, D. V. Pushkarev, G. E. Rizaev, D. V. Mokrousova, A. V. Koribut, Y. V. Grudtsyn, N. A. Panov, L. V. Seleznev, W. Liu, A. A. Ionin, and O. G. Kosareva, "Flat-top THz directional diagram of a DC-biased filament," Opt. Lett. **46**(21), 5497 (2021).
4. L. V. Seleznev, G. Rizaev, D. Pushkarev, A. Koribut, Yu. Gerasimova, Ya. Grudtsyn, S. Savinov, Yu. Mityagin, D. Mokrousova, and A. Ionin, "Frequency-angular distribution for terahertz emission of single-color laser filament plasma under an electrostatic field," J. Opt. Soc. Am. B **38**(7), 2168 (2021).
5. N. A. Panov, O. G. Kosareva, V. A. Andreeva, A. B. Savel'ev, D. S. Uryupina, R. V. Volkov, V. A. Makarov, and A. P. Shkurinov, "Angular distribution of the terahertz radiation intensity from the plasma channel of a femtosecond filament," JETP Lett. **93**(11), 638–641 (2011).
6. C. D'Amico, A. Houard, M. Franco, B. Prade, A. Mysyrowicz, A. Couairon, and V. T. Tikhonchuk, "Conical forward THz emission from femtosecond-laser-beam fifilamentation in air," Phys. Rev. Lett. **98**(23), 235002 (2007).
7. C. Liu, Y. Chen, J. Zhao, L. Tang, Y Peng, and Y. Zhu, "Plasma micro-cavity of terahertz wave during laser filamentation," IEEE Photonics J. **11**(4), 1–14 (2019).
8. Y. S. You, T. I. Oh, and K. Y. Kim, "Off-axis phase-matched terahertz emission from two-color laser-induced plasma filaments," Phys. Rev. Lett. **109**(18), 183902 (2012).
9. V. A. Andreeva, O. G. Kosareva, N. A. Panov, D. E. Shipilo, P. M. Solyankin, M. N. Esaulkov, P. González de Alaiza Martínez, A. P. Shkurinov, V. A. Makarov, L. Bergé, and S. L. Chin, "Ultrabroad Terahertz Spectrum Generation from an Air-Based Filament Plasma," Phys. Rev. Lett. **116**(6), 063902 (2016).
10. A. Gorodetsky, A. D. Koulouklidis, M. Massaouti, and S. Tzortzakis, "Physics of the conical broadband terahertz emission from two-color laser-induced plasma filaments," Phys. Rev. A **89**(3), 033838 (2014).
11. Z. Zhang, Y. Chen, M. Chen, Z. Zhang, J. Yu, Z. Sheng, and J. Zhang, "Controllable terahertz radiation from a linear-dipole array formed by a two-color laser filament in air," Phys. Rev. Lett. **117**(24), 243901 (2016).
12. D. E. Shipilo, N. A. Panov, I. A. Nikolaeva, A. A. Ushakov, P. A. Chizhov, K. A. Mamaeva, V. V. Bukin, S. V. Garnov, and O. G. Kosareva, "Low-Frequency Content of THz Emission from Two-Color Femtosecond Filament," Photonics **9**(1), 17 (2021).
13. J. Zhao, W. Chu, Z. Wang, Y. Peng, C. Gong, L. Lin, Y. Zhu, W. Liu, Y. Cheng, S. Zhuang, and Z. Xu, "Strong Spatial Confinement of Terahertz Wave inside Femtosecond Laser Filament," ACS Photonics **3**(12), 2338–2343 (2016).
14. J. F. Molloy, M. Naftaly, and R. A. Dudley, "Characterization of Terahertz Beam Profile and Propagation," IEEE J. Select. Topics Quantum Electron. **19**(1), 8401508 (2013).
15. M. T. Reiten, S. A. Harmon, and R. A. Cheville, "Terahertz beam propagation measured through three-dimensional amplitude profile determination," J. Opt. Soc. Am. B **20**(10), 2215 (2003).
16. A. Gürtler, C. Winnewisser, H. Helm, and P. U. Jepsen, "Terahertz pulse propagation in the near field and the far field," J. Opt. Soc. Am. A **17**(1), 74 (2000).
17. M. S. Kulya, V. A. Semenova, V. G. Bespalov, and N. V. Petrov, "On terahertz pulsed broadband Gauss-Bessel beam free-space propagation," Sci. Rep. **8**(1), 1390 (2018).
18. S. H. Phing, A. Mazhorova, M. Shalaby, M. Peccianti, M. Clerici, A. Pasquazi, Y. Ozturk, J. Ali, and R. Morandotti, "Sub-wavelength terahertz beam profiling of a THz source via an all-optical knife-edge technique," Sci. Rep. **5**(1), 8551 (2015).
19. J. Zhao, W. Chu, L. Guo, Z. Wang, J. Yang, W. Liu, Y. Cheng, and Z. Xu, "Terahertz imaging with sub-wavelength resolution by femtosecond laser filament in air," Sci. Rep. **4**(1), 3880 (2014).
20. J. Zhao, Q. Wang, Y. Hui, Y. Chen, Z. Jin, A. P. Shkurinov, Y. Peng, Y. Zhu, and S. L. Zhuang, "Traveling-wave antenna model for terahertz radiation from laser-plasma interactions," SciPost Phys. Core **5**(3), 046 (2022).
21. S. Freer, A. Gorodetsky, and M. Navarro-Cia, "Beam Profiling of a Commercial Lens-Assisted Terahertz Time Domain Spectrometer," IEEE Trans. Terahertz Sci. Technol. **11**(1), 90–100 (2021).
22. J. Zhao, X. Zhang, S. Li, C. Liu, Y. Chen, Y. Peng, and Y. Zhu, "Detecting the propagation effect of terahertz wave inside the two-color femtosecond laser filament in the air," Appl. Phys. B **124**(3), 45 (2018).
23. T. I. Oh, Y. J. Yoo, Y. S. You, and K. Y. Kim, "Generation of strong terahertz fields exceeding 8 MV/cm at 1kHz and real-time beam profiling," Appl. Phys. Lett. **105**(4), 041103 (2014).
24. S. M. Teo, B. K. Ofori-Okai, C. A. Werley, and K. A. Nelson, "Single-shot THz detection techniques optimized for multidimensional THz spectroscopy," Rev. Sci. Instrum. **86**(5), 051301 (2015).
25. Y. Tian, J. Liu, Y. Bai, S. Zhou, H. Sun, W. Liu, J. Zhao, R. Li, and Z. Xu, "Femtosecond-laser-driven wire-guided helical undulator for intense terahertz radiation," Nat. Photonics **11**(4), 242–246 (2017).

26. G. Liao, Y. Li, H. Liu, G. G. Scott, D. Neely, Y. Zhang, B. Zhu, Z. Zhang, C. Armstrong, E. Zemaityte, P. Bradford, P. G. Huggard, D. R. Rusby, P. McKenna, C. M. Brenner, N. C. Woolsey, W. Wang, Z. Sheng, and J. Zhang, "Multimillijoule coherent terahertz bursts from picosecond laser-irradiated metal foils," Proc. Natl. Acad. Sci. U. S. A. **116**(10), 3994–3999 (2019).

27. J. Zhao, J. Yan, Z. Dong, C. Liu, Y. Han, Y. Peng, W. Lin, and Y. Zhu, "Cladding-Free Antiresonance in Tubular Structures," Adv. Photonics Res. **3**(12), 2200148 (2022).

28. J. Zhao, J. Yan, Y. Han, L. Lao, Y. Peng, and Y. Zhu, "Paper-folding-based terahertz anti-resonant cavity," Opt. Lett. **48**(3), 704 (2023).

29. X. Zang, H. Ding, Y. Intaravanne, L. Chen, Y. Peng, J. Xie, Q. Ke, A. V. Balakin, A. P. Shkurinov, X. Chen, Y. Zhu, and S. Zhuang, "A multi-foci metalens with polarization-rotated focal points," Laser Photonics Rev. **13**, 1900182 (2019).

30. T. Hattori, H. Kumon, and H. Tamazumi, "Terahertz spectroscopic characterization of paper," in *35th International Conference on Infrared, Millimeter, and Terahertz Waves* (2010), pp. 1–2.

31. G. M. Katyba, K. I. Zaytsev, N. V. Chernomyrdin, I. A. Shikunova, G. A. Komandin, V. B. Anzin, S. P. Lebedev, I. E. Spektor, V. E. Karasik, S. O. Yurchenko, I. V. Reshetov, V. N. Kurlov, and M. Skorobogatiy, "Sapphire photonic crystal waveguides for terahertz sensing in aggressive environments," Adv. Opt. Mater. **6**(22), 1800573 (2018).

32. J. Neu and C. A. Schmuttenmaer, "Tutorial: An introduction to terahertz time domain spectroscopy (THz-TDS)," J. Appl. Phys. **124**(23), 231101 (2018).

33. B. You, J. Lu, J. Liou, C. Yu, H. Chen, T. Liu, and J. Peng, "Subwavelength film sensing based on terahertz anti-resonant reflecting hollow waveguides," Opt. Express **18**(18), 19353–19360 (2010).

34. C. Lai, B. You, J. Lu, T. Liu, J. Peng, C. Sun, and H. Chang, "Modal characteristics of antiresonant reflecting pipe waveguides for terahertz waveguiding," Opt. Express **18**(1), 309–322 (2010).

35. C. Themistos, K. Kallib, M. Komodromosa, C. Markidesa, A. Quadirc, B. M. A. Rahmanc, and K. T. V. Grattanc, "Low-loss multimode interference couplers for terahertz waves," in *the Conference on Microstructured and Specialty Optical Fibres* (2012).

36. J. Canning and A. L. G. Carter, "Modal interferometer for in situ measurements of induced core index change in optical fibers," Opt. Lett. **22**(8), 561 (1997).

37. Y. Peng, J. Huang, J. Luo, Z. Yang, L. Wang, X. Wu, X. Zang, C. Yu, M. Gu, Q. Hu, X. Zhang, Y. Zhu, and S. Zhuang, "Three-step one-way model in terahertz biomedical detection," PhotoniX **2**, 12 (2021).

38. Y. Zhu, X. Zang, H. Chi, Y. Zhou, Y. Zhu, and S. Zhuang, "Metasurfaces designed by a bidirectional deep neural network and iterative algorithm for generating quantitative field distributions," Light Adv. Manuf. **4**, 9 (2023).

39. X. Zang, B. Yao, L. Chen, J. Xie, X. Guo, A. V. Balakin, A. P. Shkurinov, and S. Zhuang, "Metasurfaces for manipulating terahertz waves," Light Adv. Manuf. **2**, 10 (2021).